# **3D PRINTING**

# Volumetric additive manufacturing via tomographic reconstruction

Brett E. Kelly<sup>1,2\*</sup>, Indrasen Bhattacharya<sup>3\*</sup>, Hossein Heidari<sup>1\*</sup>, Maxim Shusteff<sup>2</sup>, Christopher M. Spadaccini<sup>4</sup>, Hayden K. Taylor<sup>1</sup>†

Additive manufacturing promises enormous geometrical freedom and the potential to combine materials for complex functions. The speed, geometry, and surface quality limitations of additive processes are linked to their reliance on material layering. We demonstrated concurrent printing of all points within a three-dimensional object by illuminating a rotating volume of photosensitive material with a dynamically evolving light pattern. We printed features as small as 0.3 millimeters in engineering acrylate polymers and printed soft structures with exceptionally smooth surfaces into a gelatin methacrylate hydrogel. Our process enables us to construct components that encase other preexisting solid objects, allowing for multimaterial fabrication. We developed models to describe speed and spatial resolution capabilities and demonstrated printing times of 30 to 120 seconds for diverse centimeter-scale objects.

dditive manufacturing (AM) technologies are increasingly used to produce end-use, multicomponent, and multimaterial parts (1). They meet fabrication needs in applications including patient-specific medical devices (2, 3), optics (4), microfluidics (5), aerospace components (6), fixturing (7), and tooling (8). Current AM processes create three-dimensional (3D) geometries through repeated 1D or 2D unit operations (9–12). Such layer-by-layer approaches limit throughput, degrade surface quality, constrain geometric capa-

bilities, increase postprocessing requirements, and may cause anisotropy of mechanical performance. A manufacturing technique capable of simultaneously fabricating all points within an arbitrary 3D geometry would provide a different strategy to address these issues and complement existing AM methods. A method that forms parts volumetrically allows for different ways to integrate multiple components and may widen the material landscape to enhance the functionality of finished parts (*I*).

We developed a method, computed axial lithography (CAL), that allowed us to synthesize arbitrary geometries volumetrically through photopolymerization. The CAL approach has several advantages over conventional layer-based printing methods. Our method may be used to circumvent support structures, as it can print into high-viscosity fluids or even solids. Printing 3D structures around preexisting solid components is also possible with our approach. CAL is scalable to larger print volumes and is several orders of magnitude faster, under a wider range of conditions, than layer-by-layer methods.

The CAL manufacturing system we developed selectively solidifies a photosensitive liquid within a contained volume. We delivered light energy to the material volume as a set of 2D images. Each image projection propagates through the material from a different angle. The superposition of exposures from multiple angles (Fig. 1A) results in a 3D energy dose sufficient to solidify the material in the desired geometry. Our process was inspired by the image reconstruction procedures of computed tomography (CT), a technique widely used in medical imaging and nondestructive testing (13, 14). The core concepts of CT can be

<sup>1</sup>Department of Mechanical Engineering, University of California, Berkeley, Berkeley, CA 94720, USA. <sup>2</sup>Materials Engineering Division, Lawrence Livermore National Laboratory, Livermore, CA 94550, USA. <sup>3</sup>Applied Science and Technology program, University of California, Berkeley, Berkeley, CA 94720, USA. <sup>4</sup>Engineering Directorate, Lawrence Livermore National Laboratory, Livermore, CA 94550, USA. \*These authors contributed equally to this work.

†Corresponding author. Email: hkt@berkeley.edu

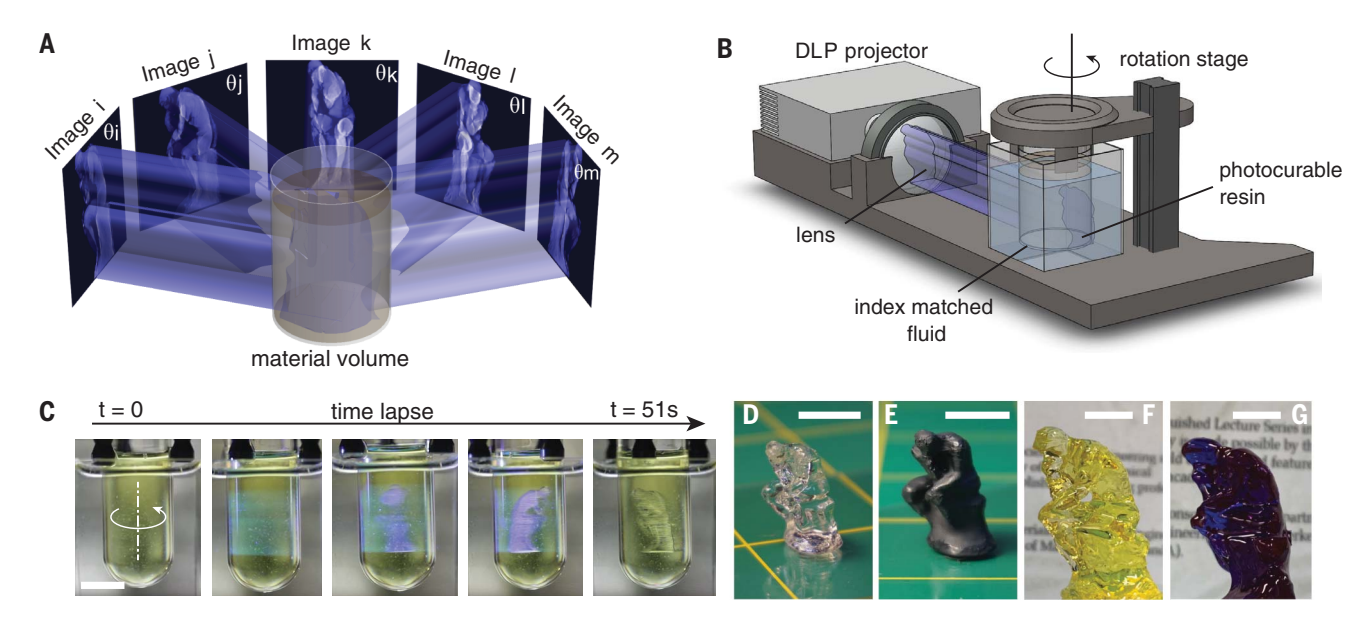


**Fig. 1. CAL volumetric fabrication.** (**A**) Underlying concept: Patterned illumination from many directions delivers a computed 3D exposure dose to a photoresponsive material. (**B**) Schematic of the CAL system used in this work. DLP projector, digital light processor–based projector. (**C**) Sequential view of the build volume during a CAL print. A 3D geometry is formed in the material in less than 1 min. (**D**) The 3D part shown in (C) after rinsing away uncured material. (**E**) The part from (D), painted for clarity. (**F**) A larger (40-mm-tall) version of the same geometry. (**G**) Opaque version of the geometry in (F), using crystal violet dye in the resin. Scale bars: 10 mm.

directly applied to additive fabrication. A related dose-delivery method is intensity-modulated radiation therapy (IMRT) for cancer treatment (15). IMRT creates a 3D exposure inside a patient's body to target tumor regions with a critical radiation dose while limiting the dose in regions containing vital organs. The CAL process is able to recover exactly the sculpted geometry (fig. S7), as the response of the material to the optical dose is nonlinear, unlike in IMRT.

We designed a physical system to fabricate 3D parts (Fig. 1B). We used a digital video projector to output our computed intensitymodulated projections, which we time-sequenced to the rotation rate of the uncured photopolymer precursor material. Free radicals are generated by light activation and then rapidly quenched and deactivated by oxygen during the initial, inhibition phase of printing (16). For the material to begin to cross-link at a given position within the volume, oxygen must be sufficiently depleted locally. The nonlinear response of the material is due to the oxygen inhibition process, which sets a critical dose threshold.

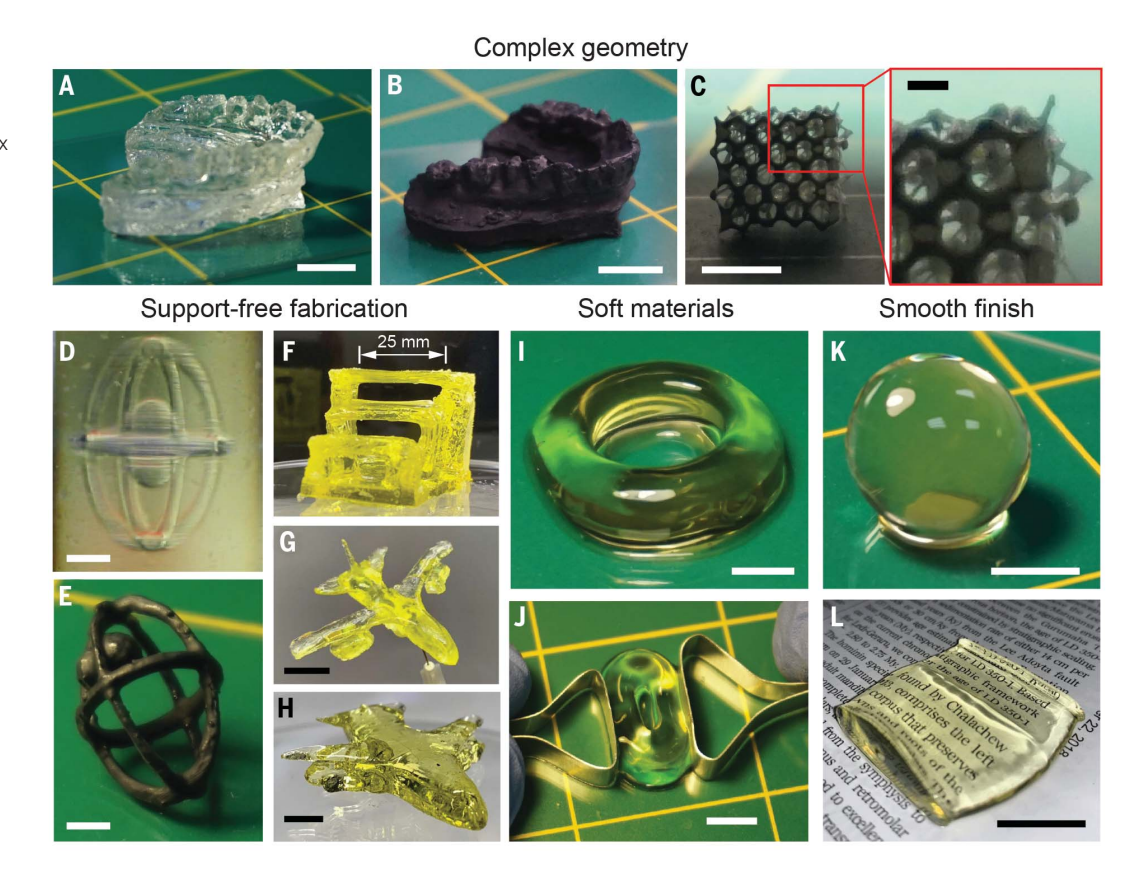
After we exposed the resin from all angles, we observed the full 3D object overcoming inhibition simultaneously and materializing as a whole within the volume (Fig. 1C). This process is a clear departure from conventional AM technologies, which build parts serially point by point or layer by layer. We used highly viscous (up to ~90,000 centipoises) or solid (thermally gelled) precursor materials to minimize relative motion between the printed object and the precursor. High-viscosity precursors also limited molecular diffusioninduced blurring. After exposure, we removed uncured material by solvent rinsing, sometimes combined with moderate heating to liquefy or reduce the viscosity of the uncured material, to liberate the structure (Fig. 1D). We further cured the 3D part after release by using light to enhance material properties (17). For material chemistries not inhibited by oxygen, we can obtain dose-response nonlinearity by adding other inhibiting molecules to the resin (18, 19). CAL requires penetration of the curing wavelength through the printing volume, but dye can be added to block other wavelengths and tune component opacity (Fig. 1, F and G).

Using commercially available projection hardware, we demonstrated the capability of our CAL system for fast build times. We completed a centimeter-scale geometry (Fig. 1, C to E) in less than 1 min. Using intensities in the range of ~0.1 to 2.0 mW/cm<sup>2</sup>, we produced a large array of geometries (Figs. 1 and 2 and fig. S3), with lateral sizes up to ~55 mm, in 30 to 300 s.

CAL is a physical implementation of the back-projection algorithm used in CT reconstruction, subject to a positivity constraint in the filtered projections (20, 21). Prior work addressing the volumetric 3D lithography problem used holography and field interference to sculpt 3D energy distributions, with compelling results on sparse or highly symmetric geometries (9, 22). However, the standard digital holography problem is ill-posed because of the dimensionality mismatch between 3D space and 2D projections (23). The mathematical framework of CT reconstruction currently allows for geometric flexibility that may be advantageous compared with that enabled by other techniques. The projection slice theorem governs the relationship between the integral projections and the Fourier transform of the desired target geometry, ensuring that the projections contain the necessary information to construct the object. This relationship underscores the generality of the CAL technique.

We computed the 3D target geometry on a Cartesian voxel basis from the standard stereolithography file format (.stl). This allowed us to use the technique on widely available, 3Dprintable, computer-aided design models. As an example, we rendered the famous Rodin sculpture, The Thinker (Fig. 3A). The z axis was parallel to the axis of rotation of the material volume shown in Fig. 1, B and C. The computation is described for a z slice of the target geometry  $f_T(\mathbf{r}, z)$ , which takes the value 1 or 0 to represent the desired presence or absence of material. In polar coordinates, the corresponding projection intensities are  $g(r, \theta, z)$ 

Fig. 2. Parts fabricated by CAL. (A) A highly complex geometry (dental model). (B) Same part as in (A), painted for clarity. (C) Complex lattice geometry with fine features as small as 0.3 mm and internal voids. (D) "Ballin-a-cage" geometry: an example of a disconnected part printed without solid support structures. The part is suspended in uncured material. (E) The part in (D), removed from uncured material and painted for clarity. (F) Bridges with unsupported spans up to 25 mm. (G and H) Airplanes with sharp wing tips and overhanging wings. (I and J) Donut printed in highly deformable GelMA hydrogel, showing a smooth, layerless surface finish. (K) Smooth sphere without layering artifacts. (L) Component with smooth planar and convex curved regions. Scale bars: 10 mm [(A), (B), and (L)]; 5 mm [(C), and (G) to (K)]; 1 mm [inset of (C)]; 2 mm [(D) and (E)].



in watts per square centimeter. We used the notation of Tretiak and Metz (24) to describe the exponential Radon transform  $T_{\alpha}[f]$  and its adjoint, the back-projection operator  $T_{\alpha}^{*}[g]$ . We expressed the physically based forward

model that transforms the intensity images into solidified resin as an exponential back-projection operator  $T^*_{-\alpha}[g]$  to produce a dose distribution (in joules per cubic centimeter), followed by a step-function curing operation at

C Α Radon  $F^{\mathsf{1D}}$ 10<sup>2</sup> 0.5  $\theta = 0$  $\pi/5$  $2\pi/5$  $3\pi/5$  $4\pi/5$ 0.5 1 0 2H/6 z=H/6 3H/6 4H/6 5H/6 G Н

**Fig. 3. Projection computation.** (**A**) 3D target object. (**B**) z cross section. (**C**) Radon transform. (**D**) 2D Fourier transform. (**E**) Integral projections at example angles. (**F**) Optimized projections. (**G**) Cumulative dose from back-projection of integral projection. (**H**) Optimized cumulative dose at the same cross sections as in (G). H is the total height of the geometry being printed, and z = 0 at the base of the geometry.

the material conversion threshold

$$\begin{split} f(\mathbf{r},z) &= I \Big\{ \frac{\alpha}{\Omega} \Big( T_{-\alpha}^*[g](\mathbf{r},z) \Big) \ge D_{\rm c} \Big\} \\ &= I \Big\{ \frac{\alpha}{\Omega} \Big( \int_{\theta=0}^{2\pi} g(\mathbf{r}.\hat{\theta},\theta,z) e^{-\alpha \mathbf{r}.\hat{\theta}_{\perp}} d\theta \Big) \ge D_{\rm c} \Big\} \end{split}$$

$$(1)$$

where I is an indicator function expressing the threshold,  $D_c$  is the critical dose that defines adequate solidification of the material,  $\alpha$ is the resin's optical absorption coefficient, and  $\Omega$  is the rotation rate of the container. The printed geometry  $f(\mathbf{r}, z)$  takes the value 0 or 1 to indicate the absence or presence, respectively, of cured material and can be directly compared with the target geometry  $f_{\rm T}$ . The coordinate system we used to express the polar unit vectors  $\hat{\theta}$  and  $\hat{\theta}_{\perp}$  is shown in Fig. 3B. We defined the intensity projections  $g(r, \theta, z)$ on radial lines through the center of the container. Our transformation to projected intensities needs to account for attenuation by the photosensitive material (17).

Our desire was to compute projections  $g(r, \theta, z)$  such that the printed geometry f closely emulates the desired target geometry  $f_T$ . The problem admits an exact solution given by the inverse exponential Radon transform of the 2D dose distribution at each z slice (24, 25). In other words, back-projecting the analytical inverse of the exponential Radon exactly produced the target geometry. We expressed the inverse through the filtered back-projection formula

$$g_{
m ont}^{\pm}(r, heta,z) = \mathcal{F}^{-1} ig\{ \hat{W}_{lpha} \hat{T}_{lpha}[f_{
m T}] ig\}$$
 (2)

where  $\mathcal{F}^{-1}$  is the inverse Fourier transform operator, and the  $\hat{T}_a$  operator is the Fourier transform of the amplified integral projection of the 2D target geometry

$$\begin{split} \hat{T}_{\alpha}[f_{\mathrm{T}}](k,\theta,z) \\ &= \int_{r} \int_{t} f_{\mathrm{T}}(r\hat{\theta} + t\hat{\theta}_{\perp}) e^{\alpha t} e^{-ikr} \mathrm{d}t \mathrm{d}r \end{split} \tag{3}$$

The symbol k is the Fourier conjugate variable to the radius  $r, t = \mathbf{r}.\hat{\theta}_{\perp}$  and  $\hat{W}_{\alpha}(k) = kI_{|k| \geq \alpha}$  is the frequency domain back-projection filter. Spatial frequencies below  $\alpha$  are zeroed (17, 24). The ramp filter behaves as a high-pass filter and introduces negative excursions to the projection images  $g_{\text{opt}}^{\pm}(r,\theta,z)$ . In the case of negligible attenuation  $(\alpha \sim 0)$ , the filter simplifies to the standard Ram-Lak filter for filtered back-projection (21). Notably, from the projection slice theorem in the  $\alpha \sim 0$  case, the 2D Fourier transform of the "flatland" target geometry for a given z slice is exactly equal to the 1D Fourier transform of the integral projections along radial samples in the Fourier domain:  $\hat{f}(\mathbf{k}, z) = \hat{T}_0[f](\mathbf{k}.\hat{\theta}, \theta, z)$ . We illustrated this in Fig. 3D, where the radial samples along the dashed lines are the 1D Fourier transform (in the radius variable) of the integral projections (Fig. 3C).

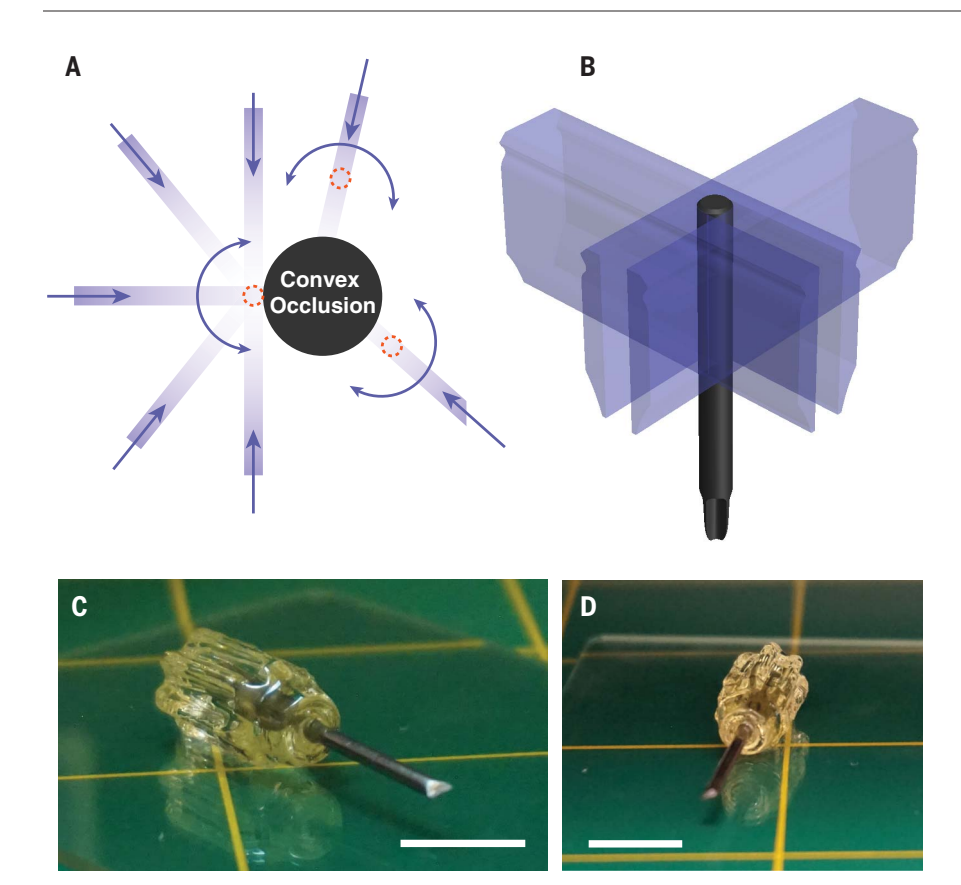


Fig. 4. CAL enables overprinting of 3D geometries around preexisting solid components. (A and B) A convex occlusion allows access from the half-space, permitting delivery of the projections needed to cure custom geometries around the occlusion. Red circles in (A) denote examples of locations around the convex geometry, which can all be addressed from the half-space of angles. (C and D) Example of a screwdriver handle printed using CAL to encase a metallic shaft. Scale bars: 10 mm.

Although  $T_{-\alpha}^*[g_{\mathrm{opt}}^{\pm}](\mathbf{r},z)$  produces the target geometry, it will, by necessity, include negative intensity values. This is a problem in radiation therapy as well, and the dose recipe is typically obtained by iterative optimization while accounting for constraints in the problem formulation (26). Because the exact solution in Eq. 3 cannot be implemented by incoherent, temporally multiplexed intensity summation from a projector, the optimal incoherent intensity projections are instead obtained by solving the 3D inverse problem

$$g_{\mathrm{opt}}(r,\theta,z) = \mathrm{argmin} \ \|f - f_{\mathrm{T}}\|_2 \qquad \ (4)$$

subject to the constraint  $g_{\text{opt}} \ge 0$  for intensityonly projections. We used an iterative optimization procedure based on projected gradient descent updates to solve Eq. 4. We found that incorporating the thresholding nonlinearity into the problem is critical to obtaining a good correspondence between the dose profile and target geometry (fig. S7).

Optimized projections for The Thinker (Fig. 3F) have sharper features than the integral projections (Fig. 3E), arising from the filtering

operation in the inverse transform. We also show the 3D dose profiles that correspond to their respective projections (Fig. 3, G and H). As expected, the dose distribution resulting from the integral projections (Fig. 3G) is blurred and fails to reproduce sharp geometric features. Further, the dose associated with z slices containing higher dc content is larger. In contrast, the integrated intensity from the optimized projections (Fig. 3H) closely matches the target geometry (black line). We used this optimization procedure to generate projection images for a wide variety of geometries that we then printed using CAL (Fig. 2 and fig. S3).

The ability to synthesize custom geometries volumetrically offers a suite of fabrication advantages over layer-based AM methods. The elimination of layering resulted in parts with exceptionally smooth surface finishes (Fig. 2, I to L). Additionally, by rapidly fabricating the entire 3D geometry concurrently, CAL required no support structures even when printing re-entrant and overhanging features (Fig. 2, D to H) or disconnected parts (Fig. 2, D and E). The system architecture employed in the CAL fabrication process also offers advantages when the converted material is of low elastic modulus, as in the ~1- to 10-kPa regime needed for many soft tissue modeling and bioprinting applications (27). We demonstrated this with 3D patterning of a gelatin methacrylate (GelMA) hydrogel material (Fig. 2, I to K, and fig. S3C). Printing this material with a layer-by-layer process would be difficult because of the forces exerted on incomplete structures during the build (17).

CAL also widens the field of photopolymers for AM by allowing the use of higher-viscosity materials. Layer-based photopolymer printing technologies typically impose a maximum viscosity limit on the prepolymer mixture to allow the resin to reflow between the printing of subsequent layers. To meet this major design constraint, photopolymer formulations are often blended with reactive diluent monomers (28) to reduce the resin viscosity. This process can adversely affect the properties of the resulting solid material. In the CAL process, more viscous materials can be used because flow of the material is not required during printing (17). CAL can thus enable printing of materials that are otherwise difficult or slow to 3D print because of their high viscosity in the precursor form. Example materials include those with high stiffness and thermal resistivity (29), along with silicones (30).

CAL is well suited for printing material around a complex, preexisting 3D structure (Fig. 4). The Radon transform possesses a 180° shift symmetry that enables printing of arbitrary geometries onto convex substrates with exposure from the half-space of angles. We synthesized a polymeric handle onto a metal screwdriver shaft (Fig. 4) to demonstrate this ability to synthesize a custom geometry onto an existing mass-manufactured part. We immersed the metal piece in the photopolymer before the rotation during printing. This methodology provides an AM technique analogous to the high-volume injection molding techniques of overmolding and insert molding. This AM capability, which we term "overprinting," opens up a wide range of possibilities for multiprocess AM. For example, overprinting could be used to encapsulate electronics, improve mechanical properties of orthodontics, or fabricate a customized exterior for an object with a mass-produced skeleton.

Our modeling of light absorption by the rotating resin volume indicates that the illumination time needed for curing can be minimized, for a given projector power, when the resin's absorption coefficient  $\alpha$  equals the reciprocal of the printing volume's radius (31). This result suggests that CAL is inherently scalable to larger print volumes, with components having diameters ~0.5 m and submillimeter features being feasible with the illumination power and resolution of a single commercially available projector. CAL's compatibility with relatively weakly optically absorbing resins, coupled with its low surface roughness, makes it particularly appealing for optical applications. These advantages, complemented by the ability to combine materials through overprinting, may motivate the integration of CAL with mass production and other AM techniques for rapid and cost-effective manufacturing of biomaterials and structures, medical and dental devices, and aerospace applications, to name a few.

### **REFERENCES AND NOTES**

- 1. E. MacDonald, R. Wicker, Science 353, aaf2093 (2016).
- 2. X. Wang et al., Biomaterials 83, 127-141 (2016).
- 3. A. Bhargav, V. Sanjairaj, V. Rosa, L. W. Feng, J. Fuh Yh, J. Biomed. Mater. Res. B 106, 2058-2064 (2018).
- 4. D. T. Nguyen et al., Adv. Mater. 29, 1701181 (2017).
- 5. H. Gong, B. P. Bickham, A. T. Woolley, G. P. Nordin, Lab Chip 17, 2899-2909 (2017).
- 6. T. D. Ngo, A. Kashani, G. Imbalzano, K. T. Q. Nguyen, D. Hui, Compos., Part B Eng. 143, 172-196 (2018).
- A. Gebhardt, J.-S. Hötter, Additive Manufacturing: 3D Printing for Prototyping and Manufacturing (Carl Hanser Verlag, 2016); www.hanser-elibrary.com/doi/book/10.3139/ 9781569905838
- 8. E. Sachs, E. Wylonis, S. Allen, M. Cima, H. Guo, Polym. Eng. Sci. 40, 1232-1247 (2000).
- 9. M. Shusteff et al., Sci. Adv. 3, eaao5496 (2017).
- 10. C. W. Hull, "Apparatus for production of three-dimensional objects by stereolithography." U.S. Patent 4,575,330 (1986)
- 11. J. R. Tumbleston et al., Science 347, 1349-1352 (2015).
- 12. P. F. Jacobs, Rapid Prototyping & Manufacturing: Fundamentals of StereoLithography (Society of Manufacturing Engineers, ed. 1, 1992).
- 13. G. N. Hounsfield, "Method and apparatus for measuring x- or  $\gamma$ -radiation absorption or transmission at plural angles and analyzing the data." U.S. Patent 3,778,614
- 14. J. Kastner, C. Heinzl, in Integrated Imaging and Vision Techniques for Industrial Inspection, Z. Liu, H. Ukida,

- P. Ramuhalli, K. Niel, Eds. (Advances in Computer Vision) and Pattern Recognition Series, Springer, 2015), pp. 227-250.
- 15. T. Bortfeld, J. Bürkelbach, R. Boesecke, W. Schlegel, Phys. Med. Biol. 35, 1423-1434 (1990).
- 16. A. K. O'Brien, C. N. Bowman, Macromolecules 39, 2501-2506 (2006).
- 17. Materials and methods are available as supplementary materials.
- 18. S. S. Cutié et al., J. Appl. Polym. Sci. 64, 577-589 (1997)
- 19. M. P. de Beer et al., Sci. Adv. 5, eaau8723 (2019).
- 20. A. C. Kak, M. Slaney, Principles of Computerized Tomographic Imaging (Society of Industrial and Applied Mathematics, 2001).
- 21. G. N. Ramachandran, A. V. Lakshminarayanan, Proc. Natl. Acad. Sci. U.S.A. 68, 2236-2240 (1971).
- 22. J. Zhang, N. Pégard, J. Zhong, H. Adesnik, L. Waller, Optica 4, 1306-1313 (2017).
- 23. R. Piestun, B. Spektor, J. Shamir, J. Opt. Soc. Am. A Opt. Image Sci. Vis. 13, 1837-1848 (1996)
- 24. O. Tretiak, C. Metz, SIAM J. Appl. Math. 39, 341-354 (1980).
- 25. F. Natterer, Inverse Probl. 17, 113-119 (2001).
- 26. M. Ehrgott, Ç. Güler, H. W. Hamacher, L. Shao, Ann. Oper. Res. 175. 309-365 (2010).
- 27. S. V. Murphy, A. Atala, Nat. Biotechnol. 32, 773-785
- 28. J. W. Lee, P. X. Lan, B. Kim, G. Lim, D.-W. Cho, Microelectron. Eng. 84, 1702-1705 (2007).
- 29. M. Hegde et al., Adv. Mater. 29, 1701240 (2017).
- 30. A. S. Wu et al., Sci. Rep. 7, 4664 (2017).
- 31. Printing-rate modeling is described in sections S18 to S21 of the supplementary materials.

### **ACKNOWLEDGMENTS**

We thank R. McLeod, R. Ng, J. Oakdale, R. Panas, L. Waller, and J. Zhang for helpful discussions. We gratefully acknowledge S. E. Arevalo for assistance with nanoindentation, A. Jordan for assistance with tensile testing, I. Ladner for assistance

with roughness measurements, and R. Weitekamp for the gift of a projector module. Funding: This work was supported by U.C. Berkeley faculty start-up funds (to H.K.T.) and by Lawrence Livermore National Laboratory Laboratory-Directed Research and Development funding 14-SI-004 (to C.M.S.) and 17-ERD-116 (to M.S.). The work was performed under the auspices of the U.S. Department of Energy by Lawrence Livermore National Laboratory under contract DE-AC52-07NA27344 (LLNL-JRNL-755660). Author contributions: H.K.T., M.S., and C.M.S. planned the research and provided the overall direction; B.E.K., H.H., H.K.T., and M.S. designed experiments; B.E.K. and H.H. conducted experiments; I.B. developed the projection computation algorithm: H.K.T. and I.B. built the process models; and all authors contributed to analysis and to writing and refining the manuscript. Competing interests: The authors are inventors on a U.S. patent application related to this work (15/593,947). All authors declare that they have no other competing interests. Data and materials availability: All data are available in the manuscript or the supplementary materials. Algorithm pseudocode is available in the supplementary materials (section S12). Source .stl files for The Thinker and dental model geometries were obtained from www.thingiverse.com/thing:34343 and www.thingiverse.com/thing:1209567, respectively (both under the CC BY 3.0 license).

# SUPPLEMENTARY MATERIALS

www.sciencemag.org/content/363/6431/1075/suppl/DC1 Materials and Methods Supplementary Text Figs. S1 to S20 Tables S1 to S3 References (32-50) Movies S1 to S5

17 August 2018; resubmitted 5 December 2018 Accepted 18 January 2019 Published online 31 January 2019 10.1126/science.aau7114